Tunneling signatures of interband coherence in dilute exciton condensates

Kryštof Kolář[1,2] and Felix von Oppen[3]

[1]*Department of Applied Physics, Aalto University School of Science, FI-00076 Aalto, Finland*

[2]*Dahlem Center for Complex Quantum Systems and Fachbereich Physik, Freie Universität Berlin, 14195 Berlin, Germany*

[3]*Dahlem Center for Complex Quantum Systems, Fachbereich Physik, and Halle-Berlin-Regensburg Cluster of Excellence CCE, Freie Universität Berlin, 14195 Berlin, Germany*

(Received 12 February 2026; revised 22 May 2026; accepted 10 August 2026; published 24 August 2026)

We theoretically investigate signatures of exciton condensation and the underlying interband coherence in scanning tunneling microscopy. We consider both monolayer and bilayer condensates in the regime of a dilute condensate of tightly bound excitons. For monolayer condensates, interband coherence is directly encoded in spatially oscillating contributions to the tunneling conductance, which break the underlying lattice symmetry. We show how scanning tunneling microscopy allows one to extract the exciton wave function. For bilayer condensates, we show that the formation of the exciton insulator is signaled by the emergence of a characteristic peak in the tunneling conductance, which can be used to extract the (local) exciton density. Our results are based on analytical considerations using a systematic solution of the mean-field equations in powers of the exciton density as well as numerical calculations.

DOI: 10.1103/mb3n-l45p

I. INTRODUCTION

Excitons—bound pairs of an electron and a hole—are expected to form spontaneously in the ground state of an intrinsic narrow-gap semiconductor if the binding energy E_b of an isolated exciton exceeds the band gap E_G between the conduction and valence bands [1–4]. When E_G is close to E_b, the exciton density n_{ex} is small and the internal structure of the excitons becomes immaterial. They realize a gas of effectively pointlike bosons, with the residual overlap of excitons inducing a finite exciton compressibility. This gas is expected to undergo Bose-Einstein condensation (BEC) at low temperatures [3]. The formation of the condensate affects the noninteracting band structure only mildly by increasing the gap E_g. However, the associated emergence of interband coherence spontaneously breaks the separate charge conservation symmetries of the conduction and valence bands, permitting exciton superflow under suitable conditions. As the exciton density increases, the system eventually crosses over into a Bardeen-Cooper-Schrieffer (BCS) regime, in which overlapping bare valence and conduction bands spontaneously develop an excitation gap.

While exciton condensates have been studied for almost sixty years, recent years have seen a surge of interest in exciton insulators driven by the emergence of materials breakthroughs. Recent work on monolayers of $ZrTe_2$ [5] and WTe_2 [6,7], bilayer transition metal dichalcogenides [8–10], and bulk $Ta_2Pd_3Te_5$ [11,12] presented evidence for exciton-insulator formation, improving upon earlier candidate materials such as Ta_2NiSe_5 [13–16] and $TiSe_2$ [17,18]. Unequivocal detection of an exciton insulator is challenging since it is a state with spontaneous mixing of conduction and valence bands [2,19,20]. If this band mixing occurs between bands with a finite momentum offset, it generically couples to the lattice [19], which can also drive band mixing. Recently, Refs. [5,21,22] cast doubt on a purely excitonic origin of the states observed in Ta_2NiSe_5 and $TiSe_2$, suggesting instead a lattice-driven mechanism. Bilayer condensates in which conduction and valence bands are localized in separate layers do not couple to the lattice [23,24], while the recent experiments on $ZrTe_2$ [5] and $Ta_2Pd_3Te_5$ [12] rely on careful modeling to preclude a lattice-driven phase. Experiments on monolayer WTe_2 [6,7] argued on the basis of transport anomalies and did not observe any lattice distortion, possibly as a result of the specific spin ordering [25].

Diverse experimental techniques were used to probe candidate materials for exciton-insulator formation. Angle-resolved photoemission spectroscopy (ARPES) [5,12,13,17,22,26] mapped band structures, and the spontaneous opening of a gap at low temperatures was taken as evidence. Bilayer systems, with extraordinary tunability afforded by bias and gate voltages [27,28], allowed for thermodynamic measurements of the exciton density as a function of the band gap E_G [8–10]. Furthermore, bilayer systems allow exciton superflow to be probed, manifesting in perfect Coulomb drag [29,30] similar to quantum Hall bilayer condensates [31–35]. Notably, global probes such as ARPES or thermodynamic and transport measurements are subject to averaging over sample inhomogeneities.

A natural local probe of exciton insulators with high spatial and energy resolution is scanning tunneling microscopy (STM). STM has so far been used in the study of excitonic

Published by the American Physical Society under the terms of the Creative Commons Attribution 4.0 International license. Further distribution of this work must maintain attribution to the author(s) and the published article's title, journal citation, and DOI.

states in a limited way, primarily to confirm a gapped state [5,6,11,12,14,26]. The usefulness of STM beyond establishing gapped states was highlighted by recent experiments. Experiments on flat-band graphene-based systems [36–38] use related signatures to probe inter-valley coherence [39–42]. This technique has been extended to bulk $Ta_2Pd_3Te_5$ [11] and WTe_2 [43,44], putative exciton insulators, to detect signatures of finite-momentum interband coherence.

In this work, we theoretically study how STM can be applied to excitonic insulators, going beyond the paradigm of establishing a gapped state. To emphasize this point, we focus on the BEC regime. In this regime, there is a gap even in the absence of exciton formation. In fact, the regime of low exciton density has two advantages compared to the BCS regime. First, the effect of exciton-lattice coupling is smaller [2], rendering a competing lattice-driven transition less likely. Second, screening effects are negligible for small electron-hole density. In contrast, screening is crucial in the BCS regime, particularly in bilayer devices, where it causes an early transition into an electron-hole plasma as the density increases [45,46]. Moreover, the BEC regime allows the mean-field equations to be solved in powers of the exciton density.

Such an expansion is meaningful when the exciton condensate satisfies two conditions. First, it must be dilute, $n_{\mathrm{ex}} a_B^2 \ll 1$, where a_B is the Bohr radius of the exciton. Second, it must also be weakly interacting, $n_{\mathrm{ex}} a^2 \ll 1$, where a is the exciton-exciton scattering length. Within mean-field theory, the scattering length is of the order a_B, and the two conditions coincide. However, mean-field theory neglects the dipole-dipole interaction between excitons [3,47]. The latter can lead to scattering lengths $a \gg a_B$, allowing dilute exciton condensates to be strongly coupled, $n_{\mathrm{ex}} a^2 \gtrsim 1$. In fact, this happens in many bilayer excitonic condensates, e.g., in GaAs-based systems [48]. In these systems, our approach provides a reference point for identifying strong-coupling effects in tunneling experiments.

Some of the most prominent recent experiments were performed on heterobilayers of transition metal dichalcogenides. In these systems, the interlayer distance is typically of the order of the Bohr radius. Thus the excitons have a small dipole moment, and the scattering length associated with the dipole-dipole interaction is also of order a_B. In these systems, the conditions for the condensate to be dilute and to be weakly coupled coincide. It is then reasonable to expect that the results of mean-field theory are qualitatively correct, with quantitative renormalizations due to the dipole-dipole interaction. Our approach is thus particularly useful in systems in which the excitons have a small dipole moment. We expect this to be the case quite generally in systems based on van der Waals heterostructures.

Tunneling signatures depend on the type of sample. In monolayer samples [Fig. 1(a)], in which excitonic coherence forms between conduction and valence bands offset by a certain momentum (so that the band gap is indirect), one expects lattice-symmetry-breaking spatial oscillations in the tunneling signal. Depending on the ordering, these occur in the spin-averaged or the spin-resolved tunneling. These oscillations reflect that the excitons are forming a coherent condensate. Importantly, we show that combining measurements of the spatially averaged and oscillatory contributions to the tunneling conductance allows the exciton wave function to be extracted. Furthermore, we predict finite peaks at the band edge in the spatially averaged tunneling conductance. This contrasts with the divergence at the gap edge found in the BCS regime. Our analytical expressions for the peaks and their shape predict sharper peaks on the side of the heavier band.

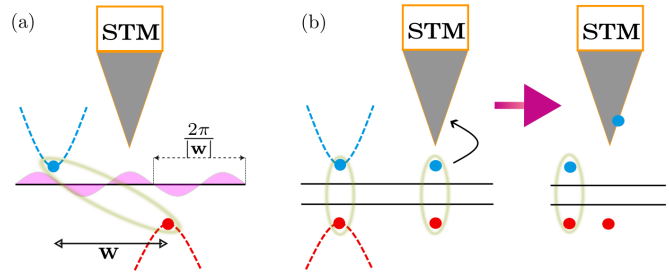


FIG. 1. (a) Schematic rendering of STM measurements on a monolayer exciton insulator. The tip is tunnel-coupled to both bands. A momentum offset between the band edges of the conduction and valence bands by a wave vector $\mathbf{w}$ leads to spatial oscillations in the STM signal with wavelength $2\pi/|\mathbf{w}|$. These are a direct signature of interband coherence. Moreover, in combination with the spatially uniform contribution to tunneling, these allow the exciton wave function to be extracted. (b) Schematic rendering of an STM experiment on a bilayer exciton condensate. The tip electrons are tunnel-coupled only to the top layer. Exciton condensation enables a process in which a conduction electron bound in an exciton tunnels out into the tip, leaving behind a valence hole. This leads to a characteristic peak in the tunneling spectrum, indicative of the formation of excitons.

In a bilayer sample, the tip electrons only couple directly to the top layer, as shown in Fig. 1(b). Assuming that the conduction band is in the top layer and the valence band in the bottom layer, there is no tunneling out of the top layer in the absence of interlayer correlations. However, such tunneling processes become possible in the exciton-insulator state, as depicted in Fig. 1(b). In the exciton insulator, an electron in the conduction band of the top layer bound into an exciton can tunnel into the tip, leaving behind a hole in the bottom layer. This process is only possible if excitons are present and leads to the emergence of a characteristic peak in the tunneling conductance upon formation of the exciton condensate. The strength of this peak can be used to extract the exciton density.

Our manuscript is structured as follows. Section II reviews the basic model of an exciton insulator, including a solution using mean-field decoupling and a low-density expansion. We also review limitations of the mean-field approach to dilute exciton condensates. In Sec. III, we formulate the framework for computing the local tunneling conductance measured by scanning tunneling microscopy. In Sec. IV, we study the tunneling signatures in a minimal model of a spinless monolayer exciton insulator, focusing on signatures of interband coherence and a method to recover the exciton wave function. Section V discusses signatures of exciton formation in bilayer condensates. In Sec. VI, we go beyond the minimal model and discuss how our results can be extended to include the effects of spin and valley degrees of freedom. Finally, we conclude in Sec. VII.

II. EXCITON CONDENSATES

A. Basic model

We begin our discussion with an elementary two-band model of exciton condensation [2,20], which neglects the spin degree of freedom. It describes the conduction and valence bands within the effective-mass approximation,

$$\epsilon^c_{\mathbf{k}} = \frac{\hbar^2\mathbf{k}^2}{2m_c} + \frac{1}{2}E_G, \tag{1}$$

$$\epsilon^v_{\mathbf{k}} = -\frac{\hbar^2\mathbf{k}^2}{2m_v} - \frac{1}{2}E_G. \tag{2}$$

We assume that the bands are isotropic with effective mass m_c (m_v) of the conduction (valence) band and separated by a band gap E_G. The momenta $\mathbf{k}$ are measured from the respective band extrema and we assume charge neutrality, with equal numbers of conduction-band electrons and valence-band holes. The corresponding Bloch functions are

$$\varphi_{\mathbf{k},i}(\mathbf{r}) = \frac{e^{i(\mathbf{k}+\mathbf{w}_i)\cdot\mathbf{r}}}{\sqrt{N_{\mathrm{UC}}}} u_{\mathbf{k}+\mathbf{w}_i,i}(\mathbf{r}), \tag{3}$$

where N_{UC} is the number of unit cells, $\mathbf{w}_i$ is the location of the band extremum of band $i = c, v$, and $u_{\mathbf{k}+\mathbf{w}_i,i}(\mathbf{r})$ is the periodic part of the Bloch function normalized within the unit cell. The conduction and valence band operators $c^\dagger_{\mathbf{k},c}$ and $c^\dagger_{\mathbf{k},v}$ are given as

$$c^\dagger_{\mathbf{k},i} = \int d\mathbf{r}\, \varphi_{\mathbf{k},i}(\mathbf{r})\psi^\dagger(\mathbf{r}), \tag{4}$$

where $\psi^\dagger(\mathbf{r})$ creates an electron at position $\mathbf{r}$. The extrema of the conduction and valence bands are offset in momentum by $\mathbf{w} = \mathbf{w}_c - \mathbf{w}_v$. With a view toward van der Waals materials, we assume the Bloch states to be perfectly localized along the z direction, with band i localized at z_i. We choose $z_c = 0$, so that $z_c = z_v = 0$ for monolayers and $z_v < 0$ for a bilayer. For this choice, the conduction-band layer is above the valence-band layer as in Fig. 1(b).

Including the Coulomb interaction, the Hamiltonian takes the form

$$H = \sum_{\mathbf{k}} \epsilon^c_{\mathbf{k}} c^\dagger_{\mathbf{k},c} c_{\mathbf{k},c} + \sum_{\mathbf{k}} \epsilon^v_{\mathbf{k}} c^\dagger_{\mathbf{k},v} c_{\mathbf{k},v} + \frac{1}{2A}\sum_{\mathbf{q}} :V^{cc}_{\mathbf{q}} \rho^c_{\mathbf{q}} \rho^c_{-\mathbf{q}} + V^{cv}_{\mathbf{q}} \rho^c_{\mathbf{q}} \rho^v_{-\mathbf{q}} + (c \leftrightarrow v): + E_C \tag{5}$$

in terms of the electron density $\rho^{c/v}_{\mathbf{q}}$ in the conduction/valence band. Here, A is the sample area, normal ordering is with respect to the intrinsic semiconductor (i.e., conduction-band electrons and valence-band holes), and $V^{ij}_{\mathbf{q}}$ is the unscreened Coulomb interaction for bands i, j,

$$V^{ij}_{\mathbf{q}} = \frac{e^2}{2\epsilon\epsilon_0|\mathbf{q}|} \exp(-|\mathbf{q}|\cdot|z_i - z_j|), \tag{6}$$

with the electron charge e, vacuum permittivity ϵ_0, and a background relative dielectric constant ϵ [49]. We included the electrostatic charging energy E_C of a parallel-plate capacitor

$$E_C = \frac{1}{2AC_G} :N^2_{\mathrm{ex}}:, \tag{7}$$

with the interlayer capacitance per unit area $C_G = \frac{\epsilon\epsilon_0}{e^2}|z_c - z_v|^{-1}$ and the exciton number operator $N_{\mathrm{ex}} = \frac{1}{2}\sum_{\mathbf{k}}(c^\dagger_{\mathbf{k},c}c_{\mathbf{k},c} - c_{\mathbf{k},v}c^\dagger_{\mathbf{k},v})$. The charging energy E_C vanishes for a monolayer condensate.

The Hamiltonian in Eq. (5) assumes the dominant-term approximation, which neglects the momentum dependence of wave-function overlaps and interband scattering [2]. In this approximation, the electron density is just the sum of the densities

$$\rho^i_{\mathbf{q}} = \sum_{\mathbf{k}} c^\dagger_{\mathbf{k},i} c_{\mathbf{k}+\mathbf{q},i} \tag{8}$$

in the two bands. Neglecting the momentum dependence of band overlaps is equivalent to approximating $u_{\mathbf{k}+\mathbf{w}_i,i}(\mathbf{r}) \simeq u_{\mathbf{w}_i,i}(\mathbf{r})$. This is justified when $u_{\mathbf{k}+\mathbf{w}_i,i}(\mathbf{r})$ is slowly varying with $\mathbf{k}$ on the scale of the inverse Bohr radius of the excitons. In what follows, we also use the simplified notation $u_{\mathbf{w}_i,i}(\mathbf{r}) \to u_i(\mathbf{r})$. In general, the electron density involves mixed terms involving both conduction and valence band operators, leading to interband scattering. For monolayer systems, these are suppressed when conduction and valence bands are offset by finite momentum $\mathbf{w}$ [Fig. 1(a)] and the Coulomb potential $V_{\mathbf{w}} \propto 1/|\mathbf{w}|$ is small relative to intraband contributions [2]. For bilayer systems with conduction and valence bands residing in different layers, the neglect of interband scattering is justified by the vanishing overlap between the conduction and valence band wave functions [24,50,51] [Fig. 1(b)].

Within the dominant-term approximation, interband scattering is neglected, and the model has separate charge-conservation symmetries for conduction and valence electrons. Interband coherence spontaneously breaks these separate symmetries, leaving only overall charge conservation. In monolayer systems, interband coherence results in spatial density modulations at the wave vector $\mathbf{w}$, forming a charge density wave (CDW) within the spinless model. The origin of this CDW is arbitrary, leading to a gapless Goldstone mode. However, interband scattering (neglected in the dominant-term approximation) explicitly breaks the separate charge conservation symmetries and generally pins the origin of the CDW, gapping out the Goldstone mode. Consequently, while monolayer exciton condensates spontaneously break the lattice translation symmetry, the independent charge conservation symmetries are explicitly broken by interband scattering terms in the interaction.

B. Mean-field solution

To set the stage, we review the mean-field solution, focusing on two dimensions. The Coulomb attraction between electrons in the conduction band and holes in the valence band leads to spontaneous condensation of electron-hole pairs (excitons) as the band gap E_G is reduced below the exciton binding energy E_b [2–4]. In the BEC limit, we can view $\sum_{\mathbf{k}} \phi_{\mathbf{k}} c^\dagger_{\mathbf{k},c} c_{\mathbf{k},v}$ as the creation operator of an exciton in the hydrogenic 1s state, where $\phi_{\mathbf{k}}$ denotes the corresponding wave function in momentum representation. We use the normalization $(1/A)\sum_{\mathbf{k}} \phi^2_{\mathbf{k}} = 1$. The corresponding Bose-condensed ground state takes the form [20]

$$|\Psi_\lambda\rangle = \exp\left(\lambda \sum_{\mathbf{k}} \phi_{\mathbf{k}} c^\dagger_{\mathbf{k},c} c_{\mathbf{k},v}\right)|\mathrm{IS}\rangle\,, \tag{9}$$

where $|\mathrm{IS}\rangle = \prod_{\mathbf{k}} c^\dagger_{\mathbf{k},v} |\mathrm{vac}\rangle$ is the ground state of the intrinsic semiconductor. The eigenvalue λ of the coherent state controls the exciton density, with the exciton density $n_{\mathrm{ex}} \simeq |\lambda|^2$ in the dilute limit [52].

More generally, the exciton wave function $\phi_{\mathbf{k}}$ can be viewed as a variational parameter [20]. Expanding the exponential, the (normalized) coherent state in Eq. (9) can be rewritten as

$$|\Psi_\lambda\rangle = \Pi_{\mathbf{k}} (u_{\mathbf{k}} c^\dagger_{\mathbf{k},v} + v_{\mathbf{k}} c^\dagger_{\mathbf{k},c}) |\mathrm{vac}\rangle , \tag{10}$$

where

$$u_{\mathbf{k}} = \frac{1}{\sqrt{1+\lambda^2\phi^2_{\mathbf{k}}}}; \quad v_{\mathbf{k}} = \frac{\lambda\phi_{\mathbf{k}}}{\sqrt{1+\lambda^2\phi^2_{\mathbf{k}}}}. \tag{11}$$

Thus the BEC ansatz is in fact a Hartree-Fock approximation in terms of the variational Slater determinant $|\Psi_\lambda\rangle$, which is not limited to the BEC limit.

The optimal Slater determinant is obtained by mean-field decoupling of the full interacting Hamiltonian of Eq. (5). This leads to the mean-field Hamiltonian [2,20,50]

$$H_{\mathrm{MF}} = \sum_{\mathbf{k},\sigma} (c^\dagger_{\mathbf{k},c} \;\; c^\dagger_{\mathbf{k},v}) h_{\mathrm{mf}} \begin{pmatrix} c_{\mathbf{k},c} \\ c_{\mathbf{k},v} \end{pmatrix}; \quad h_{\mathrm{mf}} = \begin{pmatrix} \bar{\epsilon}^c_{\mathbf{k}} & \Delta_{\mathbf{k}} \\ \Delta_{\mathbf{k}} & \bar{\epsilon}^v_{\mathbf{k}} \end{pmatrix}. \tag{12}$$

Here, the single-particle energies

$$\bar{\epsilon}^c_{\mathbf{k}} = \epsilon^c_{\mathbf{k}} - \frac{1}{A}\sum_{\mathbf{k}'} V^{cc}_{\mathbf{k}-\mathbf{k}'} \langle c^\dagger_{\mathbf{k}',c} c_{\mathbf{k}',c}\rangle + \frac{n_{\mathrm{ex}}}{2C_G}, \tag{13}$$

$$\bar{\epsilon}^v_{\mathbf{k}} = \epsilon^v_{\mathbf{k}} + \frac{1}{A}\sum_{\mathbf{k}'} V^{vv}_{\mathbf{k}-\mathbf{k}'} \langle c_{\mathbf{k}',v} c^\dagger_{\mathbf{k}',v}\rangle - \frac{n_{\mathrm{ex}}}{2C_G} \tag{14}$$

are renormalized by Fock and (for bilayer systems) interlayer capacitance terms. Moreover, $n_{\mathrm{ex}} = \langle N_{\mathrm{ex}}\rangle/A$ denotes the exciton density and

$$\Delta_{\mathbf{k}} = -\frac{1}{A}\sum_{\mathbf{k}} V^{cv}_{\mathbf{k}-\mathbf{k}'} \langle c^\dagger_{\mathbf{k}',c} c_{\mathbf{k}',v}\rangle. \tag{15}$$

measures the strength of interband coherence. We choose the order parameter to be real, which can be achieved by a suitable gauge transformation. Above, $\langle O\rangle$ denotes the expectation value of an operator O in the trial state in Eq. (10). The self-consistent ground state of Eq. (12) is the Slater determinant, which minimizes the expectation value of the full Hamiltonian [53].

According to Koopmans' theorem, the mean-field Hamiltonian h_{mf} in Eq. (12) describes the single-particle excitations [54]. This yields two bands with energies

$$E_{\mathbf{k},\pm} = \frac{\bar{\epsilon}^c_{\mathbf{k}} + \bar{\epsilon}^v_{\mathbf{k}}}{2} \pm \sqrt{\left(\frac{\bar{\epsilon}^c_{\mathbf{k}} - \bar{\epsilon}^v_{\mathbf{k}}}{2}\right)^2 + \Delta^2_{\mathbf{k}}} \tag{16}$$

and eigenvectors $(u_{\mathbf{k}}, -v_{\mathbf{k}})$ for the upper $(+)$ band and $(v_{\mathbf{k}}, u_{\mathbf{k}})$ for the lower $(-)$ band. The corresponding Bogoliubov operators are

$$d^\dagger_{\mathbf{k},+} = u_{\mathbf{k}} c^\dagger_{\mathbf{k},c} - v_{\mathbf{k}} c^\dagger_{\mathbf{k},v}, \tag{17}$$

$$d^\dagger_{\mathbf{k},-} = v_{\mathbf{k}} c^\dagger_{\mathbf{k},c} + u_{\mathbf{k}} c^\dagger_{\mathbf{k},v}. \tag{18}$$

In terms of these operators, the mean-field Hamiltonian in Eq. (12) is diagonal, $H_{\mathrm{MF}} = \sum_{\mathbf{k},\alpha=\pm} E_{\mathbf{k},\alpha} d^\dagger_{\mathbf{k},\alpha} d_{\mathbf{k},\alpha}$.

At charge neutrality, all $d^\dagger_{\mathbf{k},-}$ orbitals are occupied, while all $d^\dagger_{\mathbf{k},+}$ orbitals are empty. Thus the mean-field ground state is simply

$$\begin{aligned} |\mathrm{GS}\rangle &= \Pi_{\mathbf{k}} (u_{\mathbf{k}} c^\dagger_{\mathbf{k},v} + v_{\mathbf{k}} c^\dagger_{\mathbf{k},c}) |\mathrm{vac}\rangle \\ &= \Pi_{\mathbf{k}} (u_{\mathbf{k}} + v_{\mathbf{k}} c^\dagger_{\mathbf{k},c} c_{\mathbf{k},v}) |\mathrm{IS}\rangle , \end{aligned} \tag{19}$$

where the first line emphasizes the Hartree-Fock nature and the second the electron-hole pairing of $|\mathrm{GS}\rangle$. Using the expectation values $\langle c^\dagger_{\mathbf{k},c} c_{\mathbf{k},c}\rangle = \langle c_{\mathbf{k},v} c^\dagger_{\mathbf{k},v}\rangle = v^2_{\mathbf{k}}$ and $\langle c^\dagger_{\mathbf{k},c} c_{\mathbf{k},v}\rangle = u_{\mathbf{k}} v_{\mathbf{k}}$ in this state, the self-consistency equation reads

$$\begin{aligned} &\left(\frac{\hbar^2\mathbf{k}^2}{2m} + E_g + \frac{1}{A}\sum_{\mathbf{k}} \frac{v^2_{\mathbf{k}}}{C_G} - \frac{2}{A}\sum_{\mathbf{k}'} V^{cc}_{\mathbf{k}-\mathbf{k}'} v^2_{\mathbf{k}'}\right) u_{\mathbf{k}} v_{\mathbf{k}} \\ &\quad = \left[\frac{1}{A}\sum_{\mathbf{k}'} V^{cv}_{\mathbf{k}-\mathbf{k}'} u_{\mathbf{k}'} v_{\mathbf{k}'}\right] (u^2_{\mathbf{k}} - v^2_{\mathbf{k}}), \end{aligned} \tag{20}$$

with the reduced mass $m = m_c m_v/(m_c + m_v)$.

For both monolayers and bilayers, we will focus on the low-exciton-density (BEC) regime, where we can exploit a systematic expansion of the mean-field solution in powers of the exciton density [3,20]. For $E_G > E_b$, there is only the trivial solution $u_{\mathbf{k}} = 1$, $v_{\mathbf{k}} = 0$. For $E_G < E_b$, there will be a finite density of excitons in the ground state given by $n_{\mathrm{ex}} = (1/A)\sum_{\mathbf{k}} v^2_{\mathbf{k}}$. To lowest order in the low-density limit (small $v_{\mathbf{k}}$), Eq. (20) reduces to the excitonic Schrödinger equation [20]

$$\frac{\hbar^2 k^2}{2m} v_{\mathbf{k}} - \frac{1}{A}\sum_{\mathbf{k}'} V^{cv}_{\mathbf{k}-\mathbf{k}'} v_{\mathbf{k}'} = -E_G v_{\mathbf{k}}. \tag{21}$$

This equation is solved by setting E_G equal to the binding energy E_b of the hydrogenic 1s wave function $v_{\mathbf{k}} = \lambda\phi_{\mathbf{k}}$ in two dimensions. At this order, one recovers the coherent state in Eq. (9). In the monolayer case with $1/C_G = 0$ and a 2D Coulomb interaction, Eq. (21) can be solved analytically, giving a binding energy $E_b = 4\mathrm{Ry}^*$ and the 1s wave function

$$\phi_{\mathbf{k}} = \frac{\sqrt{2\pi} a^*_B}{[1 + (k a^*_B)^2/4]^{\frac{3}{2}}} \tag{22}$$

in terms of the excitonic Rydberg constant (Ry^*) and Bohr radius (a^*_B).

The exciton density is determined by considering higher-order contributions in Eq. (20). Expanding the energy density $\mathcal{E}$ to next order in the exciton density, one obtains

$$\mathcal{E} = (E_g - E_b) n_{\mathrm{ex}} + \frac{1}{2}\frac{d\mu_{\mathrm{ex}}}{dn_{\mathrm{ex}}} n^2_{\mathrm{ex}} \tag{23}$$

(see Appendix A). Minimizing as a function of n_{ex}, we find $E_G - E_b = \frac{d\mu_{\mathrm{ex}}}{dn_{\mathrm{ex}}} n_{\mathrm{ex}}$, where the inverse exciton compressibility $\frac{d\mu_{\mathrm{ex}}}{dn_{\mathrm{ex}}}$ can be expressed in terms of the bound-state exciton wave function $\phi_{\mathbf{k}}$ and the Coulomb interaction only. The exciton wave function $\phi_{\mathbf{k}}$ together with the exciton compressibility also enables the mean-field band energies $E_{\mathbf{k},\pm}$ to be evaluated to linear order in n_{ex}. For the monolayer wave function,

Eq. (22), the intraband Fock and pairing terms can be evaluated analytically, while the integral entering the numerical prefactor of $\frac{d\mu_{\rm ex}}{dn_{\rm ex}}$ has to be evaluated numerically.

C. Limitations of the mean-field approach

We briefly discuss two limitations of the mean-field approach to dilute exciton condensates. First, the mean-field approach retains only a repulsive contact interaction between the excitons, which results in the exciton compressibility in Eq. (23), but misses their long-range dipole-dipole interaction.

In monolayer samples, there is a van der Waals-like attraction $V_{\rm vdW}(r) \sim -A/r^6$ between excitons. Comparing potential and kinetic energy (for parabolic bands with identical band masses), the associated spatial scale is $\ell_{\rm vdW} \sim (2mA/\hbar^2)$. For hydrogenic excitons, one estimates $A \sim e^2 a_B^5$ and thus $\ell_{\rm vdW} \sim a_B$. At this level of approximation, both interactions involve the same spatial scale and compete in determining the actual exciton-exciton interaction.

In the low-density limit, the interaction can then be described by the scattering length a. As both the local repulsion and the dipole-dipole attraction involve the same spatial scale, we have $a \sim a_B$. The sign of the scattering length (and hence the exciton-exciton interaction) depends on material details, in particular the ratio of the valence- and conduction-band masses. The mean-field approach is expected to be qualitatively correct, provided that the resulting exciton-exciton interaction is repulsive. Then, the van der Waals-like dipole-dipole interaction essentially renormalizes the effective interaction obtained from the Hartree-Fock approach.

In bilayer samples, the excitons have a permanent dipole moment, which is aligned for all excitons. The dipole-dipole interaction is repulsive and falls off as $V(r) \sim e^2 d^2/r^3$ at $r \gg d$ with interlayer distance d. One extracts a characteristic length scale $a_d \sim 2me^2d^2/\hbar^2 \sim d^2/a_B$ by comparing the dipolar interaction to the kinetic energy. This gives the dimensionless parameter $r_d = (n_{\rm ex} a_d^2)^{1/2}$, implying that the dipolar repulsion dominates in the high-density limit $r_d \gg 1$, while it is effectively weak in the low-density limit, $r_d \ll 1$.

The effective strength of the dipole-dipole interaction can be parametrized by a scattering length $a \sim a_d$. For $d/a_B \gg 1$, we have $a \sim a_d \gg a_B$ so that there can be a strong-coupling regime of the dilute Bose condensate with

$$n_{\rm ex} a_B^2 \ll 1 \lesssim n_{\rm ex} a^2. \tag{24}$$

We therefore expect that the mean-field description, with appropriate renormalizations, applies only to dilute exciton systems with small interlayer distance, $d \sim a_B$. In particular, this is typically realized in heterobilayers of transition metal dichalcogenides, where $a_B, d \sim 1$nm.

Second, the mean-field approximation misses the Berezinskii-Kosterlitz-Thouless (BKT) transition in bilayer samples [55]. While electrons and holes bind into excitons below the mean-field transition temperature $T_{\rm MF} \sim \hbar^2/2ma_B^2$ governed by the interaction scale, the Berezinskii-Kosterlitz-Thouless transition occurs at the degeneracy temperature (apart from logarithmic corrections) $T_{\rm BKT} \sim \hbar^2 n_{\rm ex}/2m$. As

$$\frac{T_{\rm BKT}}{T_{\rm MF}} \sim n_{\rm ex} a_B^2, \tag{25}$$

there is a large "pseudogap" regime $T_{\rm BKT} < T < T_{\rm HF}$ in the dilute limit, where electrons and holes bind into excitons, but do not form a phase-coherent condensate. Even below $T_{\rm BKT}$, the order-parameter correlations have only quasi-long-range order. We expect that the local STM measurements which we address will be only weakly affected by the phase fluctuations of this "quasicondensate." In particular, our predictions for bilayer systems merely require pairing and should thus be largely insensitive to phase fluctuations.

III. TUNNELING CONDUCTANCE

We compute the tunneling conductance $\frac{dI}{dV}$ between tip and sample within Fermi's golden rule. It is convenient to express the conductance in terms of

$$G_0 = \frac{2\pi e^2}{\hbar} g_s t^2 \nu_0 \nu_t, \tag{26}$$

which corresponds to a spatially averaged conductance into a parabolic band (density of states $\nu_0 = m/2\pi\hbar^2$), whose mass is equal to the reduced mass m. Here, t denotes the tunneling amplitude between tip (density of states per spin ν_t) and sample, while $g_s = 2$ is a spin degeneracy factor. Apart from the replacement $m \leftrightarrow m_c$ (m_v), this corresponds to the normal-state conductance into the conduction (valence) band. Denoting the electron operator at the position $\mathbf{r}_{\rm tip}$ of the tip as $\psi(\mathbf{r}_{\rm tip})$, the zero-temperature tunneling conductance at bias voltage V can be expressed as

$$\frac{dI}{dV} = G_0 \frac{1}{\nu_0} \sum_f [|\langle f|\psi^\dagger(\mathbf{r}_{\rm tip})|{\rm GS}\rangle|^2 \delta(E_f - E_0 - eV) + |\langle f|\psi(\mathbf{r}_{\rm tip})|{\rm GS}\rangle|^2 \delta(E_0 - E_f - eV)]. \tag{27}$$

The initial state corresponds to the many-body ground state $|{\rm GS}\rangle$ with energy E_0 and we sum over all many-body final states $|f\rangle$ with energy E_f. Here, the first (second) term describes tunneling into (out of) the sample. We remark that for multilayer samples, the tip position $\mathbf{r}_{\rm tip}$ also specifies the layer into which electrons are tunneling.

Equation (27) simplifies considerably for a fermionic mean-field system. The electron operator $\psi(\mathbf{r}_{\rm tip})$ can be expanded in the band operators by inverting Eq. (4),

$$\psi^\dagger(\mathbf{r}_{\rm tip}) = \sum_{\mathbf{k}} \sum_i \varphi^*_{\mathbf{k},i}(\mathbf{r}_{\rm tip}) c^\dagger_{\mathbf{k},i}. \tag{28}$$

We can further write this in terms of the Bogoliubov operators by inverting Eq. (18). This gives

$$\psi^\dagger(\mathbf{r}_{\rm tip}) = \sum_{\mathbf{k}} \sum_{\alpha=\pm} \varphi^\dagger_{\mathbf{k}}(\mathbf{r}_{\rm tip}) \cdot \mathbf{e}_{\mathbf{k},\alpha} d^\dagger_{\mathbf{k},\alpha}. \tag{29}$$

Here, we write the Bloch functions as spinors in band space, $\varphi^T_{\mathbf{k}} = (\varphi_{\mathbf{k},c}, \varphi_{\mathbf{k},v})$ and define the unit vectors

$$\mathbf{e}_{\mathbf{k},+} = \begin{pmatrix} u_{\mathbf{k}} \\ -v_{\mathbf{k}} \end{pmatrix}; \quad \mathbf{e}_{\mathbf{k},-} = \begin{pmatrix} v_{\mathbf{k}} \\ u_{\mathbf{k}} \end{pmatrix}. \tag{30}$$

Since all $d^\dagger_{\mathbf{k},-}$ orbitals are occupied in the ground state, the sum over final states is a sum over the states $|f_{\mathbf{k},+}\rangle = d^\dagger_{\mathbf{k},+}|{\rm GS}\rangle$ for tunneling into the sample and $|f_{\mathbf{k},-}\rangle = d_{\mathbf{k},-}|{\rm GS}\rangle$ for

tunneling out of the sample. The matrix-element factors can then be written as

$$|\langle f_{\mathbf{k},+}|\,\psi^\dagger(\mathbf{r}_{\rm tip})\,|\mathrm{GS}\rangle\,|^2 = \mathrm{Tr}\,\{\Phi(\mathbf{k},\mathbf{r}_{\rm tip})P_+(\mathbf{k})\}, \tag{31}$$

$$|\langle f_{\mathbf{k},-}|\,\psi(\mathbf{r}_{\rm tip})\,|\mathrm{GS}\rangle\,|^2 = \mathrm{Tr}\,\{\Phi(\mathbf{k},\mathbf{r}_{\rm tip})P_-(\mathbf{k})\} \tag{32}$$

in terms of the Bloch-function factor

$$[\Phi(\mathbf{k},\mathbf{r}_{\rm tip})]_{i,j} = \varphi_{\mathbf{k},i}(\mathbf{r}_{\rm tip})\varphi^*_{\mathbf{k},j}(\mathbf{r}_{\rm tip}) \tag{33}$$

and the projectors

$$[P_\alpha(\mathbf{k})]_{i,j} = (\mathbf{e}_{\mathbf{k},\alpha})_i(\mathbf{e}_{\mathbf{k},\alpha})^*_j \tag{34}$$

characterizing the Bogoliubov excitations of the exciton insulator. We further neglect the weak dependence of the Bloch functions on $\mathbf{k}$, so that $\Phi(\mathbf{k},\mathbf{r}_{\rm tip})$ takes the explicit form

$$\Phi_{i,j}(\mathbf{r}_{\rm tip}) \simeq \frac{1}{N_{\rm UC}} e^{i(\mathbf{w}_i-\mathbf{w}_j)\cdot\mathbf{r}_{\rm tip}} u_{\mathbf{w}_i,i}(\mathbf{r}_{\rm tip})u^*_{\mathbf{w}_j,j}(\mathbf{r}_{\rm tip}). \tag{35}$$

The tunneling conductance can now be compactly written as

$$\frac{dI}{dV} = G_0 \frac{1}{\nu_0}\sum_{\mathbf{k},\alpha} \mathrm{Tr}\,[\Phi(\mathbf{r}_{\rm tip})P_\alpha(\mathbf{k})]\delta(E_{\mathbf{k},\alpha}-eV). \tag{36}$$

This expression separates the real-space dependence entering through the band wave functions and thus $\Phi(\mathbf{r}_{\rm tip})$ from the mean-field solution encoded by P_α. In fact, the latter is independent of the detailed wave functions when working within the dominant-term approximation.

IV. MONOLAYER CONDENSATES

For tunneling into a monolayer condensate, both the diagonal and the off-diagonal components of the Bloch-function factor $\Phi(\mathbf{r}_{\rm tip})$ contribute. While the diagonal components reflect the lattice periodicity, the off-diagonal components oscillate spatially with wave vector $\mathbf{w}$ and do not respect the lattice symmetry except in systems with a direct gap. Thus the off-diagonal contributions reflect the translation-symmetry breaking associated with the interband coherence of the exciton condensate. We can gain insight into the off-diagonal contributions by considering, say, tunneling into the sample and writing

$$d^\dagger_{\mathbf{k},+} = u_{\mathbf{k}}c^\dagger_{\mathbf{k},c} - v_{\mathbf{k}}h_{-\mathbf{k},v} \tag{37}$$

in terms of the hole operator $h_{-\mathbf{k},v} = c^\dagger_{\mathbf{k},v}$. This implies that the amplitude for tunneling into the sample involves two processes. One process adds an unbound electron to the conduction band, while the other breaks up an exciton by removing a valence-band hole, in effect also creating an unbound conduction-band electron. Both processes contribute coherently due to the condensate formation, with the interference term just corresponding to the contribution of the off-diagonal components of the Bloch-function factor $\Phi(\mathbf{r}_{\rm tip})$.

The interference terms do not contribute to the spatially averaged conductance. Noting that $\int d\mathbf{r}_{\rm tip}\Phi(\mathbf{r}_{\rm tip}) = \mathbb{1}$, one obtains

$$\overline{\frac{dI}{dV}} = G_0\frac{1}{\nu_0 A}\sum_{\mathbf{k},\alpha}\delta(E_{\mathbf{k},\alpha}-eV), \tag{38}$$

where the overline denotes the spatial average. Thus the spatially averaged conductance measures the total density of states of the mean-field spectrum.

A. Spatially averaged tunneling conductance

We can use the framework of Sec. II B to find analytical expressions for the spatially averaged tunneling conductance in the BEC limit. Using the analytical exciton wave function in Eq. (22) and working to linear order in $n_{\rm ex}$, we find that exciton condensation changes the excitation gap to

$$E_{0,+} - E_{0,-} = [4 - 6.0\tilde{n}_{\rm ex} + 16\pi\tilde{n}_{\rm ex} - 3\pi^2\tilde{n}_{\rm ex}]\,\mathrm{Ry}^*. \tag{39}$$

Here, we write the exciton density in atomic units as $\tilde{n}_{\rm ex} = n_{\rm ex}(a^*_B)^2$. The first two terms in the square brackets are the single-particle band gap $E_G = E_b - \frac{d\mu_{\rm ex}}{dn_{\rm ex}}n_{\rm ex}$, with monolayer binding energy $E_b = 4\,\mathrm{Ry}^*$ and inverse compressibility $\frac{d\mu_{\rm ex}}{dn_{\rm ex}} = 6.0\,\mathrm{Ry}^*(a^*_B)^2$. The third term accounts for the increase of the interacting gap due to the off-diagonal pairing term $\Delta_{\mathbf{k}}$ in Eq. (12). The last term is the intraband Fock term evaluated at $\mathbf{k} = 0$, which reduces the gap. In total, the formation of the exciton condensate increases the excitation gap.

Using the same expansion in the limit of small exciton densities, we can also obtain approximate expressions for $\frac{dI}{dV}$ close to the tunneling thresholds $eV = E_{0,\pm}$. We find

$$\overline{\frac{dI}{dV}} \simeq \frac{G_0\Theta(eV-E_{0,+})}{\frac{m}{m_c} + \frac{15\pi^2}{64}\tilde{n}_{\rm ex} - 4\pi\tilde{n}_{\rm ex}\left[1+\frac{m_c}{m}\frac{eV-E_{0,+}}{E_b}\right]^{-3}}, \tag{40}$$

for positive bias ($eV > 0$) and

$$\overline{\frac{dI}{dV}} \simeq \frac{G_0\Theta(E_{0,-}-eV)}{\frac{m}{m_v} + \frac{15\pi^2}{64}\tilde{n}_{\rm ex} - 4\pi\tilde{n}_{\rm ex}\left[1+\frac{m_v}{m}\frac{E_{0,-}-eV}{E_b}\right]^{-3}}. \tag{41}$$

for negative bias ($eV < 0$). In these expressions, the first term in the denominators is the single-particle contribution, the second term is a Fock mass renormalization, and the third term is due to the excitonic pairing. The last term results in a tunneling peak at the band edge. For differing conduction and valence band masses, this peak will be more pronounced on the side of the heavier band.

A numerical solution of the mean-field equations confirms these analytical expectations. Figure 2 compares the analytical results (shown in red) to numerical Hartree-Fock results (shown in blue, see Appendix B for details) for equal [Fig. 2(a)] and different [Fig. 2(b)] band masses. We find good agreement close to the band edges. In particular, the analytical results accurately capture the more pronounced effect of exciton condensation on the side of the heavier band.

Unlike in BCS theory, the differential conductance peaks at the gap edge do not diverge. This can be traced to the fact that here, the excitation gap is governed by the band edges and not by states at the Fermi energy away from the band edges as in the BCS limit.

B. Spatial oscillations of the tunneling conductance

As discussed above, the local tunneling conductance exhibits spatial oscillations with the wave vector $\mathbf{w}$ due to the formation of the exciton condensate. Thus a spatial Fourier

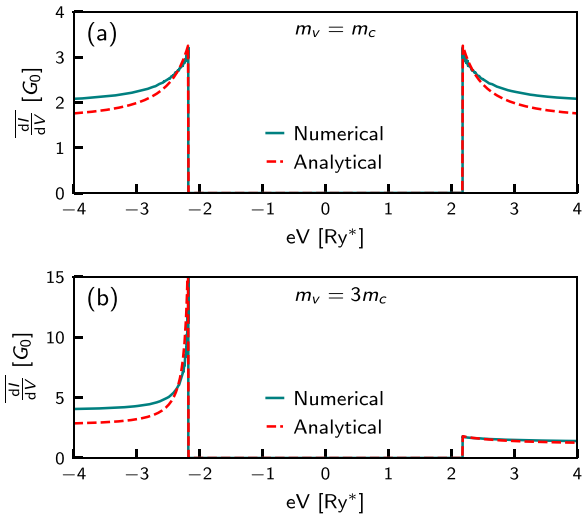


FIG. 2. Spatially averaged tunneling conductance for a monolayer; see Eq. (38). Numerical results (blue) are compared to analytical results from Eqs. (40) and (41), working at $n_{\rm ex} = 0.025\,(a_B^*)^{-2}$. The panels show results for (a) equal masses, $m_c = m_v$ and (b) unequal masses, $m_v = 3m_c$.

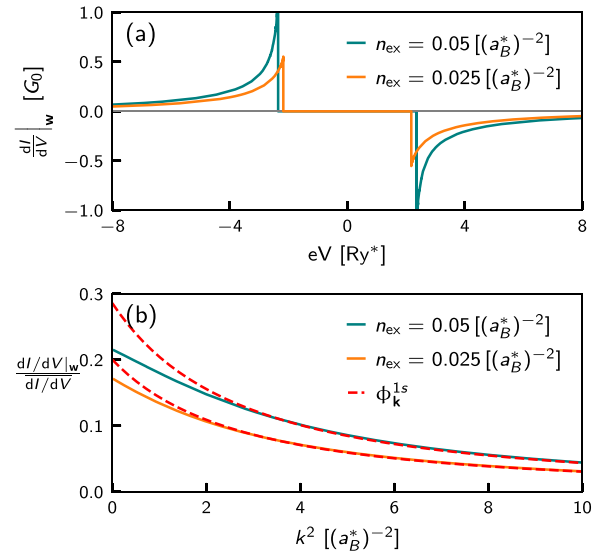


FIG. 3. (a) Fourier component of differential conductance at wave vector $\mathbf{w}$ for $n_{\rm ex}(a_B^*)^2 = 0.025$ (orange) and 0.05 (blue). (b) Exciton wave function extracted by combining numerical results for the spatially oscillating and averaged differential conductance, plotted as a function of $k^2 = \frac{e\bar{I}}{G_0\,\mathrm{Ry}^*}(a_B^*)^{-2}$, cf. Eq. (46). The dashed red line is the analytical wave function, Eq. (22), for comparison. Only a constant prefactor is fitted. Both panels: $m_c = m_v$.

transform of $\frac{dI}{dV}$ has Fourier components at wave vectors $\mathbf{w} + \mathbf{G}$, where $\mathbf{G}$ denotes the reciprocal lattice vectors. We find the explicit expressions

$$\left.\frac{dI}{dV}\right|_{\mathbf{w}+\mathbf{G}} = G_0 \frac{1}{\nu_0} \langle u_{\mathbf{w}_v,v} | u_{\mathbf{w}_c+\mathbf{G},c}\rangle \times \frac{1}{A}\sum_{\mathbf{k}} u_{\mathbf{k}} v_{\mathbf{k}} [\delta(E_{\mathbf{k},-} - eV) - \delta(E_{\mathbf{k},+} - eV)]. \tag{42}$$

Typically, the wave-function overlap $\langle u_{\mathbf{w}_v,v} | u_{\mathbf{w}_c+\mathbf{G},c}\rangle = \int_{\rm UC} d\mathbf{r}\, u_v^*(\mathbf{r}) e^{i\mathbf{G}\cdot\mathbf{r}} u_c(\mathbf{r})$ decreases rapidly with $\mathbf{G}$, implying the strongest contributions at wave vector $\mathbf{w}$. A crucial difference from the result for the spatially averaged conductance in Eq. (38) is the additional weight factor $u_{\mathbf{k}} v_{\mathbf{k}}$. Remembering that $\langle c_{\mathbf{k},c}^\dagger c_{\mathbf{k},v}\rangle = u_{\mathbf{k}} v_{\mathbf{k}}$, the spatial oscillations of the tunneling conductance are a direct signature of interband coherence. Thus these lattice-symmetry-breaking oscillations in $\frac{dI}{dV}$ are a signature of a coherent exciton condensate and would not be present for a putative incoherent exciton gas at elevated temperatures [51]. We also remark that the oscillations are analogous to the Kekulé pattern due to intervalley coherence observed recently in graphene devices [36–38].

We plot the oscillatory component in Fig. 3(a) for two representative values of the exciton density $n_{\rm ex}$, assuming a band overlap of $\langle u_{\mathbf{w}_c,c} | u_{\mathbf{w}_v,v}\rangle = \frac{1}{2}$. Due to the $u_{\mathbf{k}} v_{\mathbf{k}}$ factor, the oscillatory signal decays away from the excitation threshold on a scale given by the exciton binding energy E_b.

C. Extracting the exciton wave function

In the limit of low exciton density, the perturbative solution of the mean-field equations gives

$$\frac{1}{A} u_{\mathbf{k}} v_{\mathbf{k}} \approx \sqrt{n_{\rm ex}}\,\phi_{\mathbf{k}}^{1s}, \tag{43}$$

with the exciton wave function $\phi_{\mathbf{k}}^{1s}$ given in Eq. (22). Remarkably, this implies that measurements of the spatially averaged and spatially oscillating tunnel conductances can be combined to reconstruct the exciton wave function.

We observe that the voltage bias fixes the modulus k of the wave vector contributing to $\frac{dI}{dV}$. Thus we can extract the exciton wave function by dividing the amplitude of the spatial oscillations and the spatially averaged conductance. Working at positive bias for definiteness, we have

$$\left.\frac{\mathrm{d}I/\mathrm{d}V|_{\mathbf{w}}}{\mathrm{d}I/\mathrm{d}V}\right|_{V>0} \propto \Theta(eV - E_+^0) u_{k(V)} v_{k(V)}, \tag{44}$$

where we use Eqs. (38) and (42). The prefactor is just given by the wave-function overlap and thus independent of k.

Using rotational symmetry, the function $k(V)$ is defined implicitly through

$$E_{k(V),+} = eV, \tag{45}$$

where we assume monotonicity of $E_{k,+}$, a natural assumption in the BEC regime. To extract the change of variables from bias to momentum in experiment, one obtains the total spatially averaged current $\bar{I}(V)$ at positive bias V, e.g., by direct measurement or by integrating $\overline{\frac{dI}{dV}}$ from the conduction band bottom up to the bias V. The spatially averaged current is related to the momentum $k(V)$ through

$$\bar{I}(V) = \int_{E_+^0/e}^{E_{k(V),+}/e} dV\, \overline{\frac{dI}{dV}} = G_0 \frac{\mathrm{Ry}^*}{e} [k(V) a_B^*]^2. \tag{46}$$

Using Eq. (43), we can therefore extract the exciton wave function.

We apply this procedure to a numerical Hartree-Fock solution and show corresponding results in Fig. 3(b). Numerical

results for two different exciton densities [blue and orange lines in Fig. 3(b)] are compared to the analytical result for $\phi^{1s}_{\mathbf{k}}$ in Eq. (22) [red dashed lines in Fig. 3(b)]. For small n_{ex} (orange line), the exciton wave function can be extracted almost perfectly from this procedure. Only the overall prefactor of the wave function needs to be fitted. On the other hand, for larger n_{ex} (blue line), there are some deviations for small momenta. The deviations appear because $v_{\mathbf{k}}$ becomes significant for small momenta $\mathbf{k}$, so that assuming $u_{\mathbf{k}} \approx 1$ as in Eq. (43) is no longer valid. We conclude that the spatial oscillations in the STM measurements signal the existence of an exciton condensate. Moreover, they also enable the exciton wave functions to be recovered from experimental data, provided that the crystal symmetry is such that the conduction- and valence-band edges have approximate rotational symmetry.

V. BILAYER CONDENSATES

In bilayer systems, tunneling is only possible into, say, the top layer hosting the conduction band. This can be accounted for by setting $\varphi_{\mathbf{k},v}(\mathbf{r}_{\mathrm{tip}}) = 0$, so that the Bloch-function factor $[\Phi]_{c,c} = |\varphi_{\mathbf{k},c}(\mathbf{r}_{\mathrm{tip}})|^2$ is the only nonzero matrix element of $\Phi(\mathbf{r}_{\mathrm{tip}})$. As a result, unlike for monolayers, the tunneling conductance

$$\frac{dI}{dV} = G_0 \frac{1}{\nu_0} \sum_{\mathbf{k},\alpha} |\varphi_{\mathbf{k},c}(\mathbf{r}_{\mathrm{tip}})|^2 [P_\alpha(\mathbf{k})]_{c,c} \delta(E_{\mathbf{k},\alpha} - eV) \quad (47)$$

respects the lattice symmetry. However, bilayers still allow for an interesting signature of exciton formation. In fact, in the absence of exciton formation ($u_{\mathbf{k}} = 1$ and $v_{\mathbf{k}} = 0$), the tunneling conductance is nonzero for $eV > 0$ only. In contrast, exciton formation leads to a nonzero tunneling conductance even for $eV < 0$. In this case, only the lower quasiparticle band $\alpha = -$ contributes to the differential conductance and we find

$$\left.\frac{dI}{dV}\right|_{eV<0} = G_0 \frac{1}{\nu_0} \sum_{\mathbf{k}} |\varphi_{\mathbf{k},c}(\mathbf{r}_{\mathrm{tip}}) v_{\mathbf{k}}|^2 \delta(E_{\mathbf{k},-} - eV). \quad (48)$$

Physically, exciton formation implies the presence of conduction-band electrons bound to valence holes. These conduction-band electrons can tunnel out, leaving behind a hole excitation in the valence band, as illustrated in Fig. 1(a). We note that unlike the off-diagonal contribution to the tunneling conductance of monolayer condensates, this signature only reflects exciton formation but does not require coherence of the condensate.

Due to the absence of lattice-symmetry-breaking spatial oscillations, we focus on the spatially averaged conductance

$$\overline{\frac{dI}{dV}} = \frac{G_0}{\nu_0 A} \sum_{\mathbf{k}} \left[v^2_{\mathbf{k}} \delta(E_{\mathbf{k},-} - eV) + u^2_{\mathbf{k}} \delta(E_{\mathbf{k},+} - eV) \right]. \quad (49)$$

Here, we also include positive biases, for which the tunneling conductance involves $|u_{\mathbf{k}}|^2$. Figs. 4(a) and 4(b) show the spatially averaged conductance for two interlayer distances. As discussed above, we observe a satellite peak emerging at negative bias, which arises from the $|v_{\mathbf{k}}|^2$ term in Eq. (49). Increasing $|z_c - z_v|$ reduces the threshold E_G necessary for the onset of exciton condensation [56], so that the satellite peak and the conduction band move closer together, as seen by comparing Figs. 4(a) and 4(b).

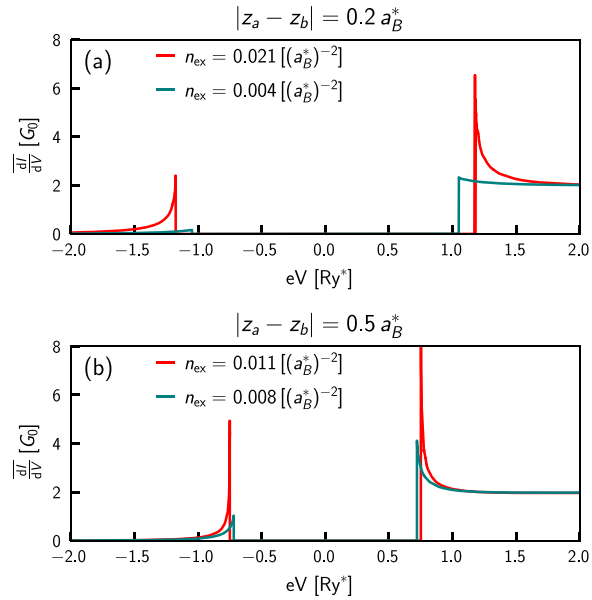


FIG. 4. (a) Spatially averaged differential conductance into a bilayer exciton condensate for $|z_a - z_b| = 0.2\, a_B^*$ for two values of n_{ex}. The appearance of a peak at negative bias is characteristic of exciton condensation. Its integrated weight provides a measure of n_{ex}, cf. Eq. (50). (b) Like (a) but with $|z_a - z_b| = 0.5\, a_B^*$. Both panels: $m_c = m_v$.

Integrating $\overline{\frac{dI}{dV}}$ across the satellite peak provides a measurement of the local exciton density in the ground state,

$$\bar{I}(V = -\infty) = \int_{E^0_-}^{-\infty} dV \, \overline{\frac{dI}{dV}} = -G_0 \frac{\mathrm{Ry}^*}{e} 4\pi n_{\mathrm{ex}}. \quad (50)$$

This may be particularly useful in inhomogeneous samples, where n_{ex} is spatially varying, so that global measurements have an inherently limited resolution. We note that the averaging in Eq. (50) serves to eliminate intra-unit-cell structure, so that it is consistent with inhomogeneities on scales large compared to the lattice spacing.

VI. SPIN- AND VALLEY DEGREES OF FREEDOM

A. Minimal model of a spinful exciton insulator

A minimal model for spinful exciton insulators [2] has spin-degenerate conduction and valence bands with independent spin-rotation symmetries. This can be thought of as two copies of the model of Sec. II. Time-reversal symmetry forces $\mathbf{w}_c$ and $\mathbf{w}_v$ to be time-reversal-invariant momenta, so that the momentum difference $\mathbf{w} = \mathbf{w}_c - \mathbf{w}_v$ is also a time-reversal-invariant momentum, which we assume to be nonzero. Using the mean-field ground state for the spinless case, Eq. (19), one mean-field charge-neutral ground state for this spinful model is simply two copies of the spinless solution,

$$|\mathrm{GS}\rangle = \Pi_{\mathbf{k},s=\uparrow,\downarrow} (u_{\mathbf{k}} + v_{\mathbf{k}} c^\dagger_{\mathbf{k},c,s} c_{\mathbf{k},v,s}) \, |\mathrm{IS}\rangle \,, \quad (51)$$

which has doubly degenerate upper and lower bands with energies given by Eqs. (16).

Using the basis $\{|\mathbf{k}, c, \uparrow\rangle, |\mathbf{k}, c, \downarrow\rangle |\mathbf{k}, v, \downarrow\rangle |\mathbf{k}, v, \downarrow\rangle\}$, the projectors onto the spin-degenerate upper and lower bands are given by a tensor product,

$$P^{\pm}_{\mathbb{1}}(\mathbf{k}) = P^{\pm}(\mathbf{k}) \otimes \mathbb{1}. \tag{52}$$

Explicitly, we have for the upper-band projector

$$P^{+}_{\mathbb{1}}(\mathbf{k}) = \begin{pmatrix} (u_{\mathbf{k}})^2 & 0 & -u_{\mathbf{k}}v_{\mathbf{k}} & 0 \\ 0 & (u_{\mathbf{k}})^2 & 0 & -u_{\mathbf{k}}v_{\mathbf{k}} \\ -u_{\mathbf{k}}v_{\mathbf{k}} & 0 & (v_{\mathbf{k}})^2 & 0 \\ 0 & -u_{\mathbf{k}}v_{\mathbf{k}} & 0 & (v_{\mathbf{k}})^2 \end{pmatrix}, \tag{53}$$

and analogously for the lower-band projector. The model has a $U(2) \times U(2)$ symmetry, so that other ground states can be generated by rotating the spin axes of conduction and valence bands. The ground-state manifold can be generated by the transformation

$$\begin{pmatrix} w & 0 \\ 0 & \mathbb{1} \end{pmatrix}, \tag{54}$$

where $w \in U(2)$ rotates the spin axis in the conduction band. The band projectors are now labeled by the matrix w and read

$$P^{\pm}_{w}(\mathbf{k}) = \begin{pmatrix} w & 0 \\ 0 & \mathbb{1} \end{pmatrix} P^{\pm}_{\mathbb{1}}(\mathbf{k}) \begin{pmatrix} w^{\dagger} & 0 \\ 0 & \mathbb{1} \end{pmatrix}. \tag{55}$$

By analyzing the energetics for different matrices in the presence of terms beyond the dominant term approximation, Halperin and Rice [2] find two candidate ground states, spin-density wave (SDW) and charge-density wave (CDW), described by

$$w_{\mathrm{SDW}} = \mathbf{n} \cdot \boldsymbol{\sigma}, \tag{56}$$

$$w_{\mathrm{CDW}} = \mathbb{1}. \tag{57}$$

The vector $\mathbf{n}$ gives the spin direction of the SDW. For weak (strong) electron-phonon coupling, the SDW (CDW) state is the ground state [2].

B. Spin-resolved tunneling

The spin structure can be probed by a tip that is partially spin polarized along a certain direction, with spin-resolved densities of states

$$\nu_{\uparrow} = \nu_t + \delta\nu/2, \tag{58}$$

$$\nu_{\downarrow} = \nu_t - \delta\nu/2. \tag{59}$$

We introduce electron operators

$$\psi^{\dagger}_{s}(\mathbf{r}_{\mathrm{tip}}) = \sum_{\mathbf{k}} \sum_{i} \phi_{\mathbf{k},i}(\mathbf{r}_{\mathrm{tip}}, s) c^{\dagger}_{\mathbf{k},i} \tag{60}$$

for the two (pseudo-)spin species $s = \uparrow / \downarrow$ of tip electrons and let the band label i also run over the spin labels. As the tunneling currents of the two spin species add, we define separate Bloch-function factors $[\Phi_s(\mathbf{r})]_{i,j} = A_{\mathrm{UC}} e^{i(\mathbf{w}_j - \mathbf{w}_i)\cdot\mathbf{r}} u^{*}_{\mathbf{w}_i,i}(\mathbf{r}, s) u_{\mathbf{w}_j,j}(\mathbf{r}, s)$ for each spin species.

We now separate the tunneling current into its contributions proportional to the average density of states ν_t as well as the density-of-states difference,

$$\frac{dI}{dV} = \frac{G_0}{\nu_0} \mathrm{Tr} \left\{ \frac{1}{A} \sum_{\mathbf{k},\alpha} P^{(\alpha)}(\mathbf{k}) \delta(E_{\mathbf{k},\alpha} - eV) \times \left[(\Phi_{\uparrow}(\mathbf{r}) + \Phi_{\downarrow}(\mathbf{r})) + \frac{\delta\nu}{2\nu_t} (\Phi_{\uparrow}(\mathbf{r}) - \Phi_{\downarrow}(\mathbf{r})) \right] \right\}. \tag{61}$$

The term proportional to $\delta\nu$ probes the spin structure of the exciton condensate. In this section, we define G_0 without the spin-degeneracy factor g_s.

C. Tunneling into the spinful model

For a tip spin polarized along $\mathbf{m}$, the matrix of wave functions is [see Eq. (35)]

$$\Phi_{\uparrow}(\mathbf{r}) + \Phi_{\downarrow}(\mathbf{r}) = \Phi^{\mathrm{spinless}}(\mathbf{r}) \otimes \mathbb{1}, \tag{62}$$

for spin-averaged tunneling and

$$\Phi_{\uparrow}(\mathbf{r}) - \Phi_{\downarrow}(\mathbf{r}) = \Phi^{\mathrm{spinless}}(\mathbf{r}) \otimes \mathbf{m} \cdot \boldsymbol{\sigma} \tag{63}$$

for the spin-polarized tunneling contribution. Here, we use the notation Φ^{spinless} for the Bloch-function factor in the spinless case, see Eq. (33). With this, the traces in Eq. (61) can be readily evaluated.

First, consider the spin-averaged tunneling. The spatial average recovers the spinless answer, measuring the total density of states as discussed in Sec. IV. In addition, there will be spatial oscillations with wave vector $\mathbf{w}$. However, due to time-reversal symmetry, $-\mathbf{w}$ and $\mathbf{w}$ are equivalent points in the Brillouin zone. Thus both off-diagonal components in Eq. (35) contribute. Accounting for this, the result for the spatially oscillating, spin-averaged component is

$$\left.\frac{dI}{dV}\right|_{\mathbf{w}} = G_0 \frac{1}{\nu_0} \langle u_v | u_c \rangle \, \mathrm{Tr}\left(w + w^{\dagger}\right) \times \frac{1}{A} \sum_{\mathbf{k}} u_{\mathbf{k}} v_{\mathbf{k}} [\delta(E_{\mathbf{k},-} - eV) - \delta(E_{\mathbf{k},+} - eV)]. \tag{64}$$

Compared to the spinless model absent time-reversal symmetry, we have the extra factor $\mathrm{Tr}\,(w + w^{\dagger})$. For the SDW state, this factor vanishes as the oscillations of the up and down spin exactly cancel. For the CDW state, on the other hand, we recover twice the result of Sec. IV B. The additional factor of two can be traced back to $-\mathbf{w}$ and $\mathbf{w}$ being equivalent momenta in this time-reversal-invariant model. As in Sec. IV C, the exciton wave function can be recovered.

The spin-polarized component can be evaluated analogously. The spatial average vanishes for all the states considered, as none of them has an overall magnetization, differing only in their interband spin correlations. There is again a spatially oscillatory component with wave vector $\mathbf{w}$, which reads

$$\left.\frac{dI}{dV}\right|_{\mathbf{w}} = G_0 \frac{1}{\nu_0} \frac{\delta\nu}{2\nu_t} \langle u_v | u_c \rangle \, \mathrm{Tr}\,[\mathbf{m} \cdot \boldsymbol{\sigma}(w + w^{\dagger})] \times \frac{1}{A} \sum_{\mathbf{k}} u_{\mathbf{k}} v_{\mathbf{k}} [\delta(E_{\mathbf{k},-} - eV) - \delta(E_{\mathbf{k},+} - eV)]. \tag{65}$$

This is nonvanishing only for the SDW order parameter, for which we have $\mathrm{Tr}\,[\mathbf{m}\cdot\boldsymbol{\sigma}(w+w^\dagger)] = 2\mathbf{m}\cdot\mathbf{n}$. The oscillating signal is maximal when the tip magnetization is aligned with the SDW direction. Again, these oscillations allow the recovery of the exciton wave function, according to the recipe of Sec. IV C.

D. Extension to multivalley systems

Systems with multiple valleys can be treated along the same lines as single-valley systems, albeit with an enlarged space of spin-valley orderings. At the level of the dominant-term approximation, the ground state can be described as a pairing between conduction and valence band flavors. If the number of conduction and valence-band valleys does not match, some flavors have to remain unpaired, and as a result, exciton condensates are only stable in the BEC regime even at the mean-field level [2].

Generically, pairing between conduction and valence bands offset by a finite momentum will lead to spatial oscillations. As an example, consider the recently studied exciton insulator candidate WTe_2 [6,7], which has two conduction-band valleys and a single valence-band valley per spin species. An analysis of the possible orders [25,57] suggests two candidate ground-state orders: a spin spiral and an SDW. Both are predicted to possess spatially dependent spin ordering, which should be observable in spin-resolved STM and allow for the recovery of wave functions as detailed in Sec. IV C. More generally, however, it is in principle possible that the spatial oscillations cancel out in the total as well as the spin-resolved tunneling conductance due to the multiple paired flavors.

VII. DISCUSSION

Tunneling experiments have long been central to the study of superconductivity. In view of the close analogies between superconductors and excitonic insulators, it is natural that tunneling experiments will also play an important role in exploring the latter. Tunneling into excitonic insulators in the limit of high exciton density (BCS limit) is closely analogous to superconductors. The formation of an excitonic insulator is signaled by the opening of a gap enclosed by divergent coherence peaks. However, this gap is expected to be strongly suppressed by screening.

Here, we focused on the limit of low exciton densities (BEC limit), a regime that is also less explored for superconductors. In this regime, exciton formation is no longer signaled by a gap opening, as even in the absence of exciton condensation, the system is a narrow-gap semiconductor. Exciton condensation merely leads to a small increase of this gap and the emergence of nondiverging peaks at the edges of the excitation gap. Nevertheless, we found that there are tunneling signatures of the formation of an exciton insulator.

In monolayers, exciton condensation is signaled by a spatially oscillating contribution to the tunneling conductance, which breaks the underlying lattice symmetry. We showed how, in the limit of low exciton density, measurements of this spatially oscillating contribution along with the spatially averaged tunneling conductance can be used to extract the exciton wave function. While spatial oscillations would also exist in the BCS limit, extracting the exciton wave function is limited to the BEC limit.

In bilayer samples, exciton formation is signaled by a characteristic peak. This peak directly reflects the presence of excitons, but is insensitive to the coherence of the condensate. Its integrated strength can be used to extract the density of excitons in the sample.

These results emphasize that STM measurements are well suited to probe exciton condensation. They enable the extraction of important information such as the exciton density and exciton wave functions. While exciton density can also be measured by alternative means, STM measurements allow it to be measured locally. STM measurements should also be valuable for probing localized in-gap states in excitonic insulators [58] as well as inelastic tunneling excitations of higher-energy states of the excitons. Moreover, they can be used to exploit sample inhomogeneity, for instance by focusing on low-disorder regions suitable for exciton condensation, a major advantage compared to spatially averaging techniques such as angle-resolved photoemission spectroscopy [5,13,17]. This may become especially powerful when combined with intentional sample engineering, enabling a wide range of model parameters to be studied in a single device [59,60].

For bilayer samples, we expect our results to be particularly relevant for systems with interlayer distances of the order of the Bohr radius, as is the case in heterobilayers of transition metal dichalcogenides. Due to dipolar exciton-exciton interactions, dilute exciton condensates can become strongly coupled for larger interlayer distances [3,47,48]. It is an interesting problem for future work to explore tunneling signatures in this limit. Another interesting open question is the effect of phase fluctuations at finite temperatures. These may also lead to inelastic contributions to the tunneling current. Moreover, the exciton condensate is expected to undergo a Berezinskii-Kosterlitz-Thouless transition and eventually turn into a classical exciton gas [20,51,61,62]. We emphasize, however, that our central prediction for bilayers, the satellite peak, should merely be thermally broadened as long as excitons are present.

ACKNOWLEDGMENTS

We are grateful to Jiewen Xiao, Daniel Muñoz-Segovia, Alexander Holleitner, and Leonid Glazman for helpful discussions. Work at Freie Universität Berlin was supported by Deutsche Forschungsgemeinschaft through CRC 183 (Project No. C02) as well as CRC 1772 (Project No. B06). Work at Aalto University was supported by a grant from the Simons Foundation (SFI-MPS-NFS-00006741-12, P.T.) in the Simons Collaboration on New Frontiers in Superconductivity.

DATA AVAILABILITY

The data that support the findings of this article are openly available [63].

APPENDIX A: PERTURBATIVE EXPANSION (DILUTE LIMIT)

We solve the self-consistency equation (20) to higher orders for small $v_{\mathbf{k}}$. The appropriate dimensionless expansion parameter is λa_B^*, with the exciton Bohr radius

$$a_B^* = \frac{4\pi\epsilon_0\epsilon\hbar^2}{e^2 m}. \tag{A1}$$

Physically, $\lambda a_B^* \ll 1$ is equivalent to $n_{\rm ex}(a_B^*)^2 \ll 1$, the limit of low exciton density.

For simplicity of notation, we write our expansion in powers of λ. According to Eq. (21), $v_{\mathbf{k}} = \lambda\phi_{\mathbf{k}}$ and $E_G = E_b$ to lowest order. We expand to higher orders as

$$v_{\mathbf{k}} = \lambda\phi_{\mathbf{k}} + \lambda^2 v_{\mathbf{k}}^{(2)} + \lambda^3 v_{\mathbf{k}}^{(3)} + \ldots, \tag{A2}$$

$$u_{\mathbf{k}} = \sqrt{1 - v_{\mathbf{k}}^2}, \tag{A3}$$

$$E_G = E_b + \lambda E_G^{(1)} + \lambda^2 E_G^{(2)} + \ldots. \tag{A4}$$

We choose functions $\phi_{\mathbf{k}}, v_{\mathbf{k}}^{(2)}, v_{\mathbf{k}}^{(3)}, \ldots$ to be orthogonal to each other.

To order λ^2, Eq. (20) reads

$$E_G^{(1)}\phi_{\mathbf{k}} + \frac{\hbar^2\mathbf{k}^2}{2m}v_{\mathbf{k}}^{(2)} - \frac{1}{A}\sum_{\mathbf{k}'} V_{\mathbf{k}-\mathbf{k}'}^{cv} v_{\mathbf{k}'}^{(2)} = -E_b v_{\mathbf{k}}^{(2)}. \tag{A5}$$

Projecting onto $\phi_{\mathbf{k}}$ and using Eq. (21), we obtain $E_G^{(1)} = 0$. This, in turn, implies with Eq. (21) that $v_{\mathbf{k}}^{(2)} \propto \phi_{\mathbf{k}}$. Hence $v_{\mathbf{k}}^{(2)}$ can be absorbed into $\phi_{\mathbf{k}}$, so that we set $v_{\mathbf{k}}^{(2)} = 0$.

To order λ^3, Eq. (20) reads

$$\begin{aligned}&\left[E_G^{(2)} + \frac{1}{A}\sum_{\mathbf{k}'}\frac{\phi_{\mathbf{k}'}^2}{C_G} - \frac{2}{A}\sum_{\mathbf{k}'}(V_{\mathbf{k}-\mathbf{k}'}^{cc}\phi_{\mathbf{k}'}^2 - \phi_{\mathbf{k}}V_{\mathbf{k}-\mathbf{k}'}^{cc}\phi_{\mathbf{k}'})\right]\phi_{\mathbf{k}} \\ &+ \left[\left(\frac{\hbar^2\mathbf{k}^2}{2m} + E_b\right)\phi_{\mathbf{k}} - \frac{1}{A}\sum_{\mathbf{k}'} V_{\mathbf{k}-\mathbf{k}'}^{cv}\phi_{\mathbf{k}'}\right]\frac{\phi_{\mathbf{k}}^2}{2} \\ &+ \frac{\hbar^2\mathbf{k}^2}{2m}v_{\mathbf{k}}^{(3)} - \frac{1}{A}\sum_{\mathbf{k}'} V_{\mathbf{k}-\mathbf{k}'}^{cv} v_{\mathbf{k}'}^{(3)} = -E_b v_{\mathbf{k}}^{(3)}.\end{aligned} \tag{A6}$$

The second line vanishes by virtue of Eq. (21). Multiplying by $\phi_{\mathbf{k}}$ and summing over $\mathbf{k}$ removes the $v_{\mathbf{k}}^{(3)}$ term, allowing $E_G^{(2)}$ to be evaluated as

$$E_G^{(2)} = -\frac{1}{C_G} + \frac{2}{A^2}\sum_{\mathbf{k},\mathbf{k}'}\left(V_{\mathbf{k}-\mathbf{k}'}^{cc}\phi_{\mathbf{k}}^2\phi_{\mathbf{k}'}^2 - \phi_{\mathbf{k}}^3 V_{\mathbf{k}-\mathbf{k}'}^{cv}\phi_{\mathbf{k}'}\right). \tag{A7}$$

Here, we used the normalization of $\phi_{\mathbf{k}}$. Noting that $n_{\rm ex} = \lambda^2 + O(\lambda^6)$, the inverse exciton compressibility $\frac{d\mu_{\rm ex}}{dn_{\rm ex}} = -\frac{dE_G}{dn_{\rm ex}} = -E_G^{(2)}$ is given by

$$\frac{d\mu_{\rm ex}}{dn_{\rm ex}} = \frac{1}{C_G} - \frac{2}{A^2}\sum_{\mathbf{k},\mathbf{k}'}\left(V_{\mathbf{k}-\mathbf{k}'}^{cc}\phi_{\mathbf{k}}^2\phi_{\mathbf{k}'}^2 - \phi_{\mathbf{k}}^3 V_{\mathbf{k}-\mathbf{k}'}^{cv}\phi_{\mathbf{k}'}\right). \tag{A8}$$

The first term is due to the geometric capacitance and reflects the dipole-dipole repulsion of excitons in bilayers. The second term is the gain of intraband exchange energy, while the last term is the interband exchange repulsion. For a monolayer, we can use the analytical form of the wave function, Eq. (22), to perform the sums over $\mathbf{k}$ and $\mathbf{k}'$. We obtain $\frac{d\mu_{\rm ex}}{dn_{\rm ex}} \approx 6.06\,{\rm Ry}^*(a_B^*)^2$.

We can also expand the energy in terms of the exciton density. For a layer-symmetric interaction, we have

$$\begin{aligned}\mathcal{E} &= \langle\Psi_\lambda|\,H\,|\Psi_\lambda\rangle \\ &= \sum_{\mathbf{k}}(\epsilon_{\mathbf{k}} + E_g)|v_{\mathbf{k}}|^2 \\ &\quad - \frac{1}{A}\sum_{\mathbf{k}}\sum_{\mathbf{k}'} V_{\mathbf{k}-\mathbf{k}'}\left[|v_{\mathbf{k}}|^2|v_{\mathbf{k}'}|^2 + u_{\mathbf{k}}^* v_{\mathbf{k}} u_{\mathbf{k}'} v_{\mathbf{k}'}^*\right].\end{aligned} \tag{A9}$$

We expand this to quartic order in $v_{\mathbf{k}}$ (using $|u_{\mathbf{k}}|^2 + |v_{\mathbf{k}}|^2 = 1$) and insert $v_{\mathbf{k}} = \sqrt{n_{\rm ex}}\phi_{\mathbf{k}}$ to obtain Eq. (23).

APPENDIX B: NUMERICAL DETAILS

Our numerical results for the coefficients $u_{\mathbf{k}}, v_{\mathbf{k}}$ are obtained by solving the mean-field Hamiltonian in Eq. (12) self-consistently. The solutions satisfy Eq. (20). We use a finite momentum grid in the radial direction, assuming that the solution is spherically symmetric (s-wave). For the monolayer case, special care needs to be taken to ensure proper convergence in view of the singular nature of the Coulomb potential. We choose grids that are sufficiently dense and large so that the exciton density is within 2% of the prediction of Eq. (A8), i.e., $\mu_{\rm ex} = 6.0566{\rm Ry}^*(a_B^*)^2 n_{\rm ex}$. Specifically, we choose a grid of $N_k = 6839$ points going up to $k_{\rm max} = 180\frac{1}{a_B^*}$ for Figs. 2 and 3. For the bilayer calculation presented in Fig. 4, we use $N_k = 1139$ points going up to $k_{\rm max} = 60\frac{1}{a_B^*}$. The exact grids are included in the dataset on Zenodo [63].

[1] D. Jérome, T. M. Rice, and W. Kohn, Excitonic insulator, Phys. Rev. **158**, 462 (1967).

[2] B. I. Halperin and T. M. Rice, The excitonic state at the semiconductor-semimetal transition, J. Phys. C: Solid State Phys. **21**, 115 (1968).

[3] L. V. Keldysh and A. N. Kozlov, Collective properties of excitons in semiconductors, Zh. Eksp. Teor. Fiz. **54**, 978 (1968) [Sov. J. Exp. Theor. Phys. **27**, 521 (1968)].

[4] A. N. Kozlov and L. A. Maksimov, The metal-dielectric divalent crystal phase transition, J. Exptl. Theoret. Phys. **48**, 1184 (1965) [Sov. Phys JETP **21**, 790 (1965)].

[5] Q. Gao, Y.-h. Chan, Y. Wang, H. Zhang, P. Jinxu, S. Cui, Y. Yang, Z. Liu, D. Shen, Z. Sun, J. Jiang, T. C. Chiang, and P. Chen, Evidence of high-temperature exciton condensation in a two-dimensional semimetal, Nat. Commun. **14**, 994 (2023).

[6] Y. Jia, P. Wang, C.-L. Chiu, Z. Song, G. Yu, B. Jäck, S. Lei, S. Klemenz, F. A. Cevallos, M. Onyszczak, N. Fishchenko, X. Liu, G. Farahi, F. Xie, Y. Xu, K. Watanabe, T. Taniguchi, B. A. Bernevig, R. J. Cava, L. M. Schoop, *et al.*, Evidence for a monolayer excitonic insulator, Nat. Phys. **18**, 87 (2022).

[7] B. Sun, W. Zhao, T. Palomaki, Z. Fei, E. Runburg, P. Malinowski, X. Huang, J. Cenker, Y.-T. Cui, J.-H. Chu, X. Xu, S. S. Ataei, D. Varsano, M. Palummo, E. Molinari, M. Rontani, and D. H. Cobden, Evidence for equilibrium exciton condensation in monolayer WTe_2, Nat. Phys. **18**, 94 (2022).

[8] L. Ma, P. X. Nguyen, Z. Wang, Y. Zeng, K. Watanabe, T. Taniguchi, A. H. MacDonald, K. F. Mak, and J. Shan, Strongly correlated excitonic insulator in atomic double layers, Nature (London) **598**, 585 (2021).

[9] Z. Wang, D. A. Rhodes, K. Watanabe, T. Taniguchi, J. C. Hone, J. Shan, and K. F. Mak, Evidence of high-temperature exciton condensation in two-dimensional atomic double layers, Nature (London) **574**, 76 (2019).

[10] R. Qi, A. Y. Joe, Z. Zhang, Y. Zeng, T. Zheng, Q. Feng, J. Xie, E. Regan, Z. Lu, T. Taniguchi, K. Watanabe, S. Tongay, M. F. Crommie, A. H. MacDonald, and F. Wang, Thermodynamic behavior of correlated electron-hole fluids in van der Waals heterostructures, Nat. Commun. **14**, 8264 (2023).

[11] M. S. Hossain, Z.-J. Cheng, Y.-X. Jiang, T. A. Cochran, S.-B. Zhang, H. Wu, X. Liu, X. Zheng, G. Cheng, B. Kim, Q. Zhang, M. Litskevich, J. Zhang, J. Liu, J.-X. Yin, X. P. Yang, J. D. Denlinger, M. Tallarida, J. Dai, E. Vescovo, *et al.*, Topological excitonic insulator with tunable momentum order, Nat. Phys. **21**, 1250 (2025).

[12] J. Huang, B. Jiang, J. Yao, D. Yan, X. Lei, J. Gao, Z. Guo, F. Jin, Y. Li, Z. Yuan, C. Chai, H. Sheng, M. Pan, F. Chen, J. Liu, S. Gao, G. Qu, B. Liu, Z. Jiang, Z. Liu, *et al.*, Evidence for an excitonic insulator state in $Ta_2Pd_3Te_5$, Phys. Rev. X **14**, 011046 (2024).

[13] K. Seki, Y. Wakisaka, T. Kaneko, T. Toriyama, T. Konishi, T. Sudayama, N. L. Saini, M. Arita, H. Namatame, M. Taniguchi, N. Katayama, M. Nohara, H. Takagi, T. Mizokawa, and Y. Ohta, Excitonic Bose-Einstein condensation in Ta_2NiSe_5 above room temperature, Phys. Rev. B **90**, 155116 (2014).

[14] Q. He, X. Que, L. Zhou, M. Isobe, D. Huang, and H. Takagi, Tunneling-tip-induced collapse of the charge gap in the excitonic insulator Ta_2NiSe_5, Phys. Rev. Res. **3**, L032074 (2021).

[15] Y. F. Lu, H. Kono, T. I. Larkin, A. W. Rost, T. Takayama, A. V. Boris, B. Keimer, and H. Takagi, Zero-gap semiconductor to excitonic insulator transition in Ta_2NiSe_5, Nat. Commun. **8**, 14408 (2017).

[16] K. Kim, H. Kim, J. Kim, C. Kwon, J. S. Kim, and B. J. Kim, Direct observation of excitonic instability in Ta_2NiSe_5, Nat. Commun. **12**, 1969 (2021).

[17] H. Cercellier, C. Monney, F. Clerc, C. Battaglia, L. Despont, M. G. Garnier, H. Beck, P. Aebi, L. Patthey, H. Berger, and L. Forró, Evidence for an excitonic insulator phase in $1T$-$TiSe_2$, Phys. Rev. Lett. **99**, 146403 (2007).

[18] A. Kogar, M. S. Rak, S. Vig, A. A. Husain, F. Flicker, Y. I. Joe, L. Venema, G. J. MacDougall, T. C. Chiang, E. Fradkin, J. van Wezel, and P. Abbamonte, Signatures of exciton condensation in a transition metal dichalcogenide, Science **358**, 1314 (2017).

[19] K. Rossnagel, On the origin of charge-density waves in select layered transition-metal dichalcogenides, J. Phys.: Condens. Matter **23**, 213001 (2011).

[20] C. Comte and P. Nozières, Exciton Bose condensation : The ground state of an electron-hole gas - I. Mean field description of a simplified model, J. Phys. France **43**, 1069 (1982).

[21] L. Windgätter, M. Rösner, G. Mazza, H. Hübener, A. Georges, A. J. Millis, S. Latini, and A. Rubio, Common microscopic origin of the phase transitions in Ta_2NiS_5 and the excitonic insulator candidate Ta_2NiSe_5, npj Comput. Mater. **7**, 210 (2021).

[22] E. Baldini, A. Zong, D. Choi, C. Lee, M. H. Michael, L. Windgaetter, I. I. Mazin, S. Latini, D. Azoury, B. Lv, A. Kogar, Y. Su, Y. Wang, Y. Lu, T. Takayama, H. Takagi, A. J. Millis, A. Rubio, E. Demler, and N. Gedik, The spontaneous symmetry breaking in Ta_2NiSe_5 is structural in nature, Proc. Natl. Acad. Sci. USA **120**, e2221688120 (2023).

[23] P. B. Littlewood and X. Zhu, Possibilities for exciton condensation in semiconductor quantum-well structures, Phys. Scr. **T68**, 56 (1996).

[24] S. Gupta, A. Kutana, and B. I. Yakobson, Heterobilayers of 2D materials as a platform for excitonic superfluidity, Nat. Commun. **11**, 2989 (2020).

[25] Y. H. Kwan, T. Devakul, S. L. Sondhi, and S. A. Parameswaran, Theory of competing excitonic orders in insulating WTe_2 monolayers, Phys. Rev. B **104**, 125133 (2021).

[26] J. Lee, C.-J. Kang, M. J. Eom, J. S. Kim, B. I. Min, and H. W. Yeom, Strong interband interaction in the excitonic insulator phase of Ta_2NiSe_5, Phys. Rev. B **99**, 075408 (2019).

[27] M. Xie and A. MacDonald, Electrical reservoirs for bilayer excitons, Phys. Rev. Lett. **121**, 067702 (2018).

[28] Y. Zeng and A. H. MacDonald, Electrically controlled two-dimensional electron-hole fluids, Phys. Rev. B **102**, 085154 (2020).

[29] R. Qi, A. Y. Joe, Z. Zhang, J. Xie, Q. Feng, Z. Lu, Z. Wang, T. Taniguchi, K. Watanabe, S. Tongay, and F. Wang, Perfect Coulomb drag and exciton transport in an excitonic insulator, Science **388**, 278 (2025).

[30] P. X. Nguyen, L. Ma, R. Chaturvedi, K. Watanabe, T. Taniguchi, J. Shan, and K. F. Mak, Perfect Coulomb drag in a dipolar excitonic insulator, Science **388**, 274 (2025).

[31] J. Eisenstein, Exciton condensation in bilayer quantum Hall systems, Annu. Rev. Condens. Matter Phys. **5**, 159 (2014).

[32] D. Nandi, A. D. K. Finck, J. P. Eisenstein, L. N. Pfeiffer, and K. W. West, Exciton condensation and perfect Coulomb drag, Nature (London) **488**, 481 (2012).

[33] M. Kellogg, J. P. Eisenstein, L. N. Pfeiffer, and K. W. West, Vanishing Hall resistance at high magnetic field in a double-layer two-dimensional electron system, Phys. Rev. Lett. **93**, 036801 (2004).

[34] E. Tutuc, M. Shayegan, and D. A. Huse, Counterflow measurements in strongly correlated GaAs hole bilayers: Evidence for electron-hole pairing, Phys. Rev. Lett. **93**, 036802 (2004).

[35] L. Du, X. Li, W. Lou, G. Sullivan, K. Chang, J. Kono, and R.-R. Du, Evidence for a topological excitonic insulator in InAs/GaSb bilayers, Nat. Commun. **8**, 1971 (2017).

[36] X. Liu, G. Farahi, C.-L. Chiu, Z. Papic, K. Watanabe, T. Taniguchi, M. P. Zaletel, and A. Yazdani, Visualizing broken symmetry and topological defects in a quantum Hall ferromagnet, Science **375**, 321 (2022).

[37] H. Kim, Y. Choi, E. Lantagne-Hurtubise, C. Lewandowski, A. Thomson, L. Kong, H. Zhou, E. Baum, Y. Zhang, L. Holleis, K. Watanabe, T. Taniguchi, A. F. Young, J. Alicea, and S. Nadj-Perge, Imaging inter-valley coherent order in magic-angle twisted trilayer graphene, Nature (London) **623**, 942 (2023).

[38] K. P. Nuckolls, R. L. Lee, M. Oh, D. Wong, T. Soejima, J. P. Hong, D. Călugăru, J. Herzog-Arbeitman, B. A. Bernevig, K. Watanabe, T. Taniguchi, N. Regnault, M. P. Zaletel, and

A. Yazdani, Quantum textures of the many-body wavefunctions in magic-angle graphene, Nature (London) **620**, 525 (2023).

[39] D. Călugăru, N. Regnault, M. Oh, K. P. Nuckolls, D. Wong, R. L. Lee, A. Yazdani, O. Vafek, and B. A. Bernevig, Spectroscopy of twisted bilayer graphene correlated insulators, Phys. Rev. Lett. **129**, 117602 (2022).

[40] J. P. Hong, T. Soejima, and M. P. Zaletel, Detecting symmetry breaking in magic angle graphene using scanning tunneling microscopy, Phys. Rev. Lett. **129**, 147001 (2022).

[41] Y. H. Kwan, G. Wagner, T. Soejima, M. P. Zaletel, S. H. Simon, S. A. Parameswaran, and N. Bultinck, Kekulé spiral order at all nonzero integer fillings in twisted bilayer graphene, Phys. Rev. X **11**, 041063 (2021).

[42] N. Bultinck, E. Khalaf, S. Liu, S. Chatterjee, A. Vishwanath, and M. P. Zaletel, Ground state and hidden symmetry of magic angle graphene at even integer filling, Phys. Rev. X **10**, 031034 (2020).

[43] M. Papaj, Spectroscopic signatures of excitonic order on quantum spin Hall edge states, Phys. Rev. B **110**, 165422 (2024).

[44] L. Watson, J. Ripoll, Z. Tong, A. Kumar, Y. Que, Y.-H. Chan, H. Lin, S. Mukherjee, M. Garnica, M. T. Edmonds, M. Papaj, A. L. Vazquez de Parga, B. Weber, I. Di Bernardo, and M. S. Fuhrer, Observation of the charge density wave excitonic order parameter in topological insulator monolayer WTe_2, ACS Nano **19**, 32374 (2025).

[45] R. Maezono, P. López Ríos, T. Ogawa, and R. J. Needs, Excitons and biexcitons in symmetric electron-hole bilayers, Phys. Rev. Lett. **110**, 216407 (2013).

[46] S. De Palo, F. Rapisarda, and G. Senatore, Excitonic condensation in a symmetric electron-hole bilayer, Phys. Rev. Lett. **88**, 206401 (2002).

[47] Y. E. Lozovik and V. I. Yudson, Feasibility of superfluidity of paired spatially separated electrons and holes; a new superconductivity mechanism, Zh. Eksp. Teor. Fiz. **22**, 556 (1975) [JETP Lett. **22**, 274 (1975)].

[48] Y. E. Lozovik, I. Kurbakov, G. Astrakharchik, J. Boronat, and M. Willander, Strong correlation effects in 2D Bose–Einstein condensed dipolar excitons, Solid State Commun. **144**, 399 (2007).

[49] For a more quantitative theory, one should also include dielectric effects due to the polarizability of the intrinsic semiconductor. This can be done using the Rytova-Keldysh potential [64,65] corresponding to the dielectric function $\epsilon(\mathbf{q}) = 1 + qr_0$, where the characteristic length $r_0 \sim e^2/\epsilon E_g$ parametrized the polarizability of the intrinsic semiconductor.

[50] X. Zhu, P. B. Littlewood, M. S. Hybertsen, and T. M. Rice, Exciton condensate in semiconductor quantum well structures, Phys. Rev. Lett. **74**, 1633 (1995).

[51] M. M. Fogler, L. V. Butov, and K. S. Novoselov, High-temperature superfluidity with indirect excitons in van der Waals heterostructures, Nat. Commun. **5**, 4555 (2014).

[52] Strictly speaking, there is no Bose condensation in the absence of interactions in a homogeneous two-dimensional system. Here, the wave function in Eq. (9) merely motivates the more general variational Hartree-Fock ansatz in Eq. (10) for the interacting system. For a more complete discussion of the nature of exciton condensation in two dimensions, see Refs. [24,51].

[53] V. Fock, Näherungsmethode zur Lösung des quantenmechanischen Mehrkörperproblems, Z. Phys. **61**, 126 (1930).

[54] T. Koopmans, Über die Zuordnung von Wellenfunktionen und Eigenwerten zu den einzelnen Elektronen eines Atoms, Physica **1**, 104 (1934).

[55] In monolayer samples, electron and hole numbers are not conserved when going beyond the dominant-term approximation. In this case, the formation of the exciton condensate only involves breaking of the discrete lattice translation symmetry by the formation of a density wave of charge, spin, or magnetization current. This does not occur via a BKT transition and is easily pinned in real samples by residual disorder.

[56] F.-C. Wu, F. Xue, and A. H. MacDonald, Theory of two-dimensional spatially indirect equilibrium exciton condensates, Phys. Rev. B **92**, 165121 (2015).

[57] Y.-Q. Wang, M. Papaj, and J. E. Moore, Breakdown of helical edge state topologically protected conductance in time-reversal-breaking excitonic insulators, Phys. Rev. B **108**, 205420 (2023).

[58] S. Kwon, K.-H. Jin, J. E. Han, S. Lee, C. Won, S.-W. Cheong, and H. W. Yeom, Yu-Shiba-Rusinov bound states of exciton condensate, arXiv:2512.23724.

[59] Z. Zhang, J. Xie, W. Zhao, R. Qi, C. Sanborn, S. Wang, S. Kahn, K. Watanabe, T. Taniguchi, A. Zettl, M. Crommie, and F. Wang, Engineering correlated insulators in bilayer graphene with a remote Coulomb superlattice, Nat. Mater. **23**, 189 (2024).

[60] L. Gu, J. Zhu, L. Zhang, S. Felsenfeld, B. Gao, R. Ma, K. Watanabe, T. Taniguchi, J. Hone, C. R. Dean, D. Xiao, and X. Xu, Remote imprinting of moiré lattices, Nat. Mater. **23**, 219 (2024).

[61] X. Zhu, M. S. Hybertsen, and P. B. Littlewood, Electron-hole system revisited: A variational quantum Monte Carlo study, Phys. Rev. B **54**, 13575 (1996).

[62] K. Asano and T. Yoshioka, Exciton–Mott physics in two-dimensional electron–hole systems: Phase diagram and single-particle spectra, J. Phys. Soc. Jpn. **83**, 084702 (2014).

[63] K. Kolář and F. von Oppen, Dataset for tunneling signatures of interband coherence in dilute exciton condensates, [Dataset], Zenodo, 2026, https://doi.org/10.5281/zenodo.18322790.

[64] N. S. Rytova, Screened potential of a point charge in a thin film, Moscow Univ. Phys. Bull. **3**, 30 (1967).

[65] L. V. Keldysh, Coulomb interaction in thin semiconduc- tor and semimetal films, Zh. Eksp. Teor. Fiz. **29**, 716 (1979) [JETP Lett. **29**, 658 (1979)].